Air entrainment and granular bubbles generated by a jet of grains entering water

A. M. Cervantes-Álvarez[1], Y. Y. Escobar-Ortega[1], A. Sauret[2] and F. Pacheco-Vázquez[1*]

[1] *Instituto de Física, Benemérita Universidad Autónoma de Puebla, Apartado Postal J-48, Puebla 72570, Mexico*

[2] *Department of Mechanical Engineering, University of California, Santa Barbara, CA, USA*

Abstract

Hypothesis. A water jet penetrating into a water pool produces air entrainment and bubbles that rise to the surface and disintegrate. A similar scenario can be expected when a granular jet enters into water. This phenomenon is common in natural and industrial processes but remains so far unexplored.
Experiments. A collimated jet of monodisperse silica beads was poured into water and the process was filmed with a high speed camera. The grain size, jet impact velocity and the liquid physical properties were systematically varied.
Findings. For grains of $\sim 50 - 300$ μm in diameter, the granular jet deforms the air-water interface, penetrates the pool and produces air entrainment. Most entrained air is that contained in the interstitial space of the jet, and its volume is linearly proportional to the volume of grains. The bubbles formed in this process are covered by a layer of grains attached to the bubble air-water interface due to capillary-induced cohesion. These "granular bubbles" are stable over time because the granular shell prevents coalescence and keeps the air encapsulated, either if the bubbles rise to the surface or sink to the bottom of the pool, which is determined by the competition of the buoyancy and the weight of the assembly.
Keywords: Granular jet, Air entrainment, Bubbles, Coalescence, gas storage, bubble stabilization, granular encapsulates, self-assembled structures.

[1] Corresponding author: *fpacheco@ifuap.buap.mx, Phone: (+52) 222.229.56.10

1. Introduction

Air entrainment produced by a water jet penetrating into a water reservoir is a common phenomenon in nature. For instance, underwater bubbles are produced due to the air entrained by waterfalls and breaking waves [1]. Controlling air entrainment is of relevance in several industrial processes, like oxidation, decarbonation and bacteria control [2]; also in hydraulic engineering, where bubbles cavitation may damage fast rotating structures [3]. Individual water drops impacting a liquid pool can also generate air entrainment [4, 5]. In fact, the familiar noise of natural rain is produced by the collapse of an air cavity generated after the impact of each raindrop and not by the impact itself [6, 7]. Perhaps, the most simple and commom exhibition of air entrainment is observed when filling a glass with water [8]. For a smooth laminar water jet, the glass can be filled without forming bubbles. When the jet becomes unstable at larger flow rates, air is entrained forming a biphasic conical region of downward bubbles that recirculate and emerge to the surface where they rapidly coalesce and disintegrate [8]. The prediction of the air entrainment conditions for plunging jets has generated an impressive amount of research [1, 8, 9, 10]. For short water jets, it has been proposed that the minimal conditions for air entrainment are satisfied for Reynolds and capillary numbers $Re > 2,000$ and $Ca > 0.04$, respectively [11], which can be expressed in terms of the Weber number as $We > Re \cdot Ca \sim O(10^2)$ [11, 12]. The precise threshold conditions of air entrainment for a continuous water jet remain elusive [9, 1].

The process of air entrainment becomes more complex when solid particles penetrate into water, even for the case of a single sphere [13, 14]. Different industrial and natural scenarios involve the discharge of discrete particles into a liquid; for instance, when pouring cement into water for mortar preparation [15], also during the natural generation of tsunami waves by landslides [16], in washing processes with powder detergents, or in our daily lives, when we pour sugar, cereal or coffee powder into a bowl with milk or water. Air entrainment and bubbles formation can occur in all these processes and it seems to depend on the size and density of the grains, the grains impact velocity, the geometry of the jet, and the liquid properties. Nevertheless, a systematic study of this scenario is missing in the literature.

When solid particles are in contact with an air-water interface, the existence of a triple liquid-solid-air contact line induces cohesive forces [17, 18, 19]. These forces are responsible for the surprising stability of sandcastles [20] and granular stalagmites [21, 22]. Capillary forces can also induce the attachment of particles to droplets and bubbles, see Fig. 1(a). For instance, pickering emulsions contain oil droplets coated by a close-packed layer of nanoparticles [23]. At a larger scale, liquid marbles are liquid droplets (usually mixtures of water and glycerol) encapsulated with hydrophobic powder within an air enviroment [24, 25, 26], gas marbles are tiny air pockets covered by a shell of glass beads joined by surfactant (SDS) liquid bridges [27], and armored droplets are encapsulates produced in microfluidic channels that enclose a fluid within a colloidal shell of micrometric-sized beads [28, 29, 30]. Armored droplets can also be produced by destabilizing a granular raft that floats at the interface between oil and water [31, 32]. All these granular encapsulates have potential applications for water storage, gas encapsulation, biomedicine, cosmetics and new aerated materials [33].

In this article we focus on two aspects of the entry of a granular jet into water: 1) the air entrained by the granular jet, so far unexplored in the literature, and 2) the formation of stable air bubbles fully covered with grains produced during the process, called here *granular bubbles*. We observe that, under certain experimental conditions, the jet of grains deforms the air-water interface leading to air entrainment and bubbles formation [Fig.1(b)]. The granular bubbles form due to the attachment of particles to the bubble air-water interface (see Movie 1 [34]). These self-assembled encapsulates can either rise to the surface or sink to the bottom of the pool [Fig. 1(c)] and remain stable during hours or even days. To explore the mechanism of air entrainment and the formation, size and stability of the bubbles, we systematically varied the grain size, the volume of poured grains, the jet impact velocity and the physical properties of the liquid.

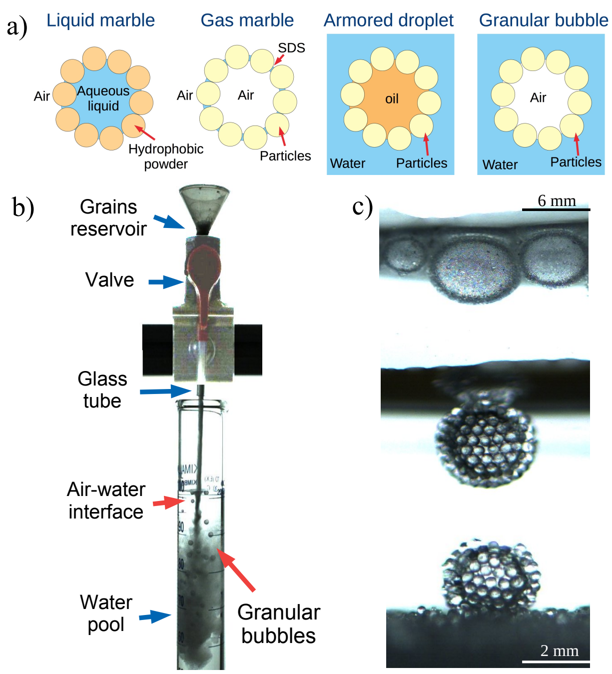

Figure 1: (a) Different types of granular encapsulates depending on the nature of the encapsulated fluid, the cohesive layer of particles and the surrounding fluid. Granular bubbles are the encapsulates studied here. (b) Experimental setup. (c) Granular bubbles produced by glass beads of radius $R_g = 25$ μm (top), 125 μm (middle) and 150 μm (bottom). As shown, the bubbles can float or sink into the water pool.

2. Materials and methods

Before each experiment, a graduated Pyrex cylinder of volume 100 mℓ is filled with deionized water. A mass $m \in [0.5,\, 6.0]\,$g corresponding to a volume $V_{grains} \in [0.2,\, 2.3]\,\mathrm{cm}^3$ of dry Ballotini® spherical glass beads (supplied by Potters Industries LLC) of a given radius $R_g \in [25,\, 225]\,\mu$m, and density $\rho_g = 2.6$ g/cm^3 is deposited in a hopper located at a height h above the water level, as illustrated in Fig. 1(b). When the valve is opened, the grains fall through a vertical glass tube of 4 mm inner diameter and length $h - 1$ cm forming a collimated dry granular jet that reaches the water surface with a velocity

$v_j \approx \sqrt{2gh}$. The jet penetration and the subsequent bubble formation are filmed with a high-speed camera Photron UX-100 at 1000 fps. By increasing h from 4 cm up to 61 cm, we varied the jet impact velocity in the range $0.9\,\mathrm{m.s^{-1}} < v_j < 3.5\,\mathrm{m.s^{-1}}$. The water temperature T was varied by previously heating the water in a hot plate. Each experiment was performed at fixed T (monitored with a thermocouple) in the range of $5°\mathrm{C} < T < 90°\mathrm{C}$ to systematically decrease the surface tension σ in the range $0.075 - 0.060$ N/m and the dynamic viscosity η in the range $1.5 - 0.32\,\mathrm{mPa.s}$ [35, 36]. These liquid properties were also varied using three binary mixtures of water with low mole fractions of ethanol X: pure water, a mixture of 95 ml water and 5 ml ethanol that corresponds to $X(5\%) = 0.016$, and a mixture of 90 ml water plus 10 ml ethanol corresponding to $X_{ethanol}(10\%) = 0.033$. For the range $0 < X < 0.033$, the value of σ decreases from 0.072 N/m to ~ 0.053 N/m, while η increases from 1 to 1.3 mPa.s [36, 37].

m ($\pm$0.01 g)	$\mathbf{R_g}$ (μm)	**T** ($\pm 1°$C)	**h** ($\pm$0.1 cm)	**X**	**Quantity measured**
2.0	25, 50, 75 100, 125, 150 175, 200	5, 10, 20, 30 40, 50, 60 70, 80, 90	7.5	0.000	R_b
2.0	25, 50, 75, 100 125, 150, 175, 200	20	4, 7.5, 11 21, 31, 61	0.000	R_b
2.0	50	20	7.5	0.000 0.016 0.033	R_b
0.5, 1.0, 1.5 2.0, 3.0, 4.0 5.0, 6.0	75, 125 150, 200	20	4, 7.5, 11 21, 31, 61	0.000	V_{air}

Table 1: Summary of the experimental parameters varied in this study: m represents the mass of poured grains, R_g the grain radius, T the water temperature, h represents the impact height and X the ethanol concentration when using binary mixtures. When it is not specified in the text or plots, the standard values $m = 2.0$ g, $R_g = 50$ μm, $T = 20°$C, $h = 7.5$ cm and $X = 0$ (pure water) must be assumed. The last column indicates the output measured in each experiment: the volume of entrained air, V_{air}, and the bubble radius, R_b.

Table 1 summarizes all the values of the five parameters varied in this study. For each experiment, four parameters are fixed and the remaining one is systematically varied, a video is taken and subsequently analyzed using ImageJ® to determine the volume of entrained air and the size of the granular bubbles.

3. Results and Discussion

3.1. Phenomenology.

Let us first describe our observations on the mechanism that leads to air entrainment and bubbles formation. Figure 2(a) shows the entrance of a collimated granular jet made of 100 μm particles poured from $h = 7.5$ cm into water at $T = 20°$C. When the jet impacts the pool, it deforms the air-water interface. The slender structure made of grains and air penetrates at high speed into the liquid, and the relative motion of the jet with respect to the quiescent liquid generates instabilities that induce the buckling of the jet. At this point, the jet breaks up in a mixture of air bubbles and grains, some grains sink individually into the pool while others attach to the bubbles surface, leading to the formation of granular bubbles that keep the entrained air encapsulated.

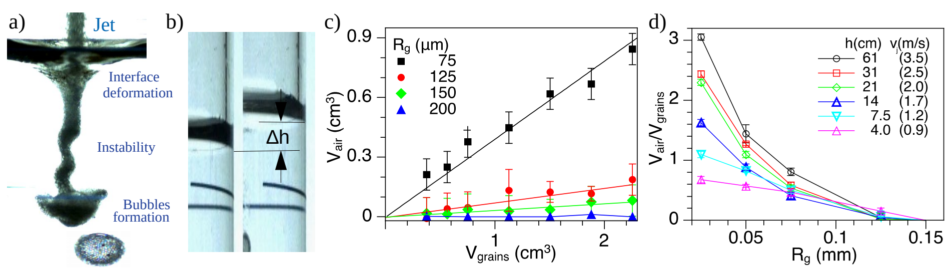

Figure 2: Air entrainment: a) Picture of a granular jet entering into water. b) Example of the change in the water level Δh produced when a given volume of glass beads is poured into the pool. c) V_{air} vs V_{grains} for different grain radii ($h = 7.5$ cm, $T = 20°$C). d) V_{air}/V_{grains} vs R_g for different impact heights ($m = 0.5$ g, $T = 20°$C). The corresponding impact velocity $v_j = \sqrt{2gh}$ is also indicated.

3.2. Air entrainment

For granular jets impacting at low speeds, images as the one shown in Fig. 2a reveal that the air entrained surrounding the jet is negligible. This suggests that the entrained air is mainly in the interstitial space of the jet. If one considers that the total volume of the jet is the volume of grains V_{grains} plus the volume of the interstitial air V_{air}, then the volume fraction of the collimated jet is given by: $\phi = V_{grains}/(V_{grains} + V_{air})$. Solving for V_{air} one finds: $V_{air} = \frac{1-\phi}{\phi} V_{grains}$. Thus, V_{air} is expected to increase linearly with V_{grains}. Experimentally, we estimated V_{air} by measuring the change in the water level Δh (see Fig. 2b) produced after pouring a given volume of grains $V_{grains} = m/\rho_g$ into the graduated cylinder of known internal cross section A. Since the total volume change is $\Delta V = V_{air} + V_{grains} = A\Delta h$, we easily determined V_{air} and it was plotted as a function of V_{grains} in Fig. 2(c). Indeed, a linear dependence is approximately found in the studied range. For $R_g = 75$ μm, the best fit gives a slope $s = (1-\phi)/\phi = 0.4$, which corresponds to a grain volume fraction $\phi = 0.71$. Although possible for spherical beads (the hexagonal close-packing of monodisperse spheres is ~ 0.74), this value of ϕ is too large considering that confined granular jets are expected to have at most a volume fraction $\phi \sim 0.60$ [38]. This indicates that an important volume of interstitial air is not trapped into bubbles during the penetration of the jet. Moreover, Fig. 2(d) shows that the ratio V_{air}/V_{grains}: i) decreases as the grain size increases, and ii) increases when the impact velocity v_j is increased [34]. One possible explanation for these dependences is that the liquid can percolate faster through larger grains because the permeability is larger according to Darcy's law; thus, the liquid invades faster the interstitial space decreasing V_{air}. For large impact velocities, the liquid has less time to percolate into the granular structure and more interstitial air is dragged within the jet during its penetration into the liquid bath. Additionally, the jet generates turbulence that promotes air entrainment as in the case of a liquid jet [10]. Nevertheless, V_{air}/V_{grains} becomes negligible for $R_g > 150$ μm regardless of v_j. As we discuss in the following sections, this grain size threshold is related with the required conditions for the generation of granular bubbles.

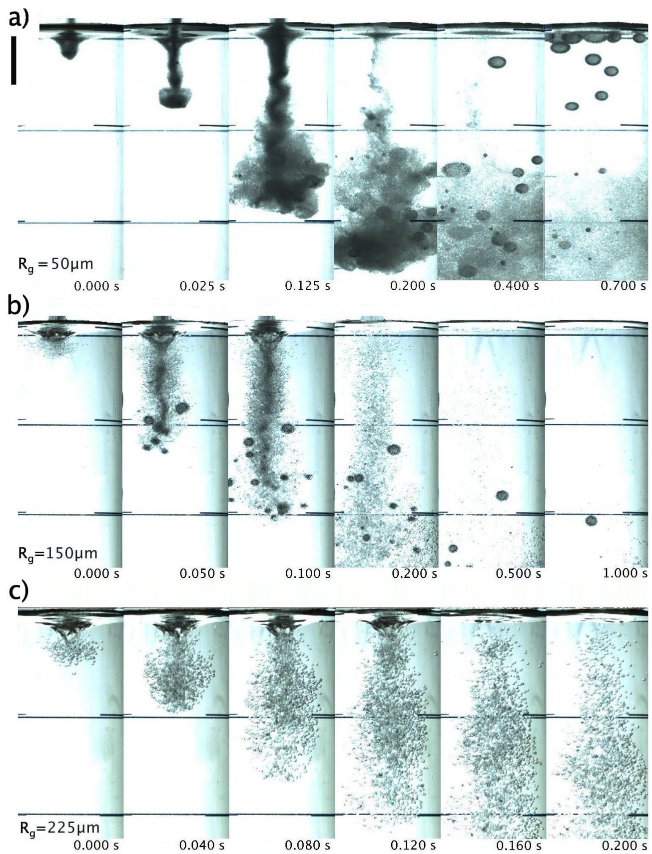

Figure 3: a) Effect of the grain radius R_g on the bubble size: for $R_g = 50$ μm, large granular bubbles rise to the water surface. For $R_g = 150$ μm, the bubbles are smaller and sink to the bottom of the pool. For $R_g = 225$ μm, bubbles are not produced. The scale bar corresponds to 10 mm. See Movie 2 in Ref. [34].

3.3. Formation of Granular Bubbles

i) Effect of grain size. Figure 3 shows examples of the jet penetration for a mass $m = 0.5$ g of grains of three different radii. For $R_g \approx 50\mu$m, the jet deforms the air-water interface and penetrates the pool forming a collimated serpentine of grains and interstitial air. Inside the water, the destabilization of the granular jet leads to the formation of air bubbles covered by grains that rise to the surface of the pool. As the grain size increases (see the case $R_g = 150$ μm) more grains are scattered across the interface, the serpentine is less pronounced and the amount of air entrained in the underwater granular jet is less significant. As a result, we observe less granular bubbles which are also considerably smaller and sink to the bottom of the pool instead of rising. For much larger grains (see the case $R_g = 225$ μm), the jet is scattered at the air-water interface, the grains penetrate the pool practically without entraining air and submerge individually. Consequently, the serpentine is not observed and granular bubbles are not produced during the process. In Refs. [38, 39], it was found that dry glass beads flowing out from a funnel form a smooth and collimated jet falling through the air if the grain size d and the funnel outlet size D satisfies the relation $D/d \gtrsim 15$; otherwise, the flow of grains becomes dispersed. If we do the calculations for our case considering that $D = 4$ mm and $d = 2R_g$, one finds $D/2R_g \approx 40$ for $R_g = 50 \mu$m, while $D/2R_g \approx 8$ for $R_g = 225$ μm. Therefore, a collimated jet is indeed expected for the smallest grains and a dispersed jet for the larger ones, in agreement with our observations in Figs. 3(a)-(c), respectively. For the intermediate value $R_g = 150$ μm (Fig. 3b), part of the jet at the center is still composed of collimated grains and can form a few smaller bubbles. Note also that $D/d = 15$ corresponds to $R_g = 133$ μm; therefore, the formation of granular bubbles is expected for grains of radius $R_g = 25, 50, 75$ and 125 μm following the above criterion. It is important to remark that the collimated jet is able to deform the surface and produce the entrainment of enough interstitial air to generate granular bubbles, whereas the air entrained by a jet of dispersed grains is negligible and bubbles do not form.

ii) Effect of the liquid properties. The volume of entrained air and the size of air bubbles generated by a plunging liquid jet penetrating a pool of the same liquid depends on the surface tension σ and viscosity η of the liquid [1]. To explore the role of these parameters in the formation of granular bubbles produced by the jet of grains, we first varied the water temperature. For pure water, the dependence of σ and η on T is shown in Figs. 4(a)-(b). Figure 4(c) shows pictures of bubbles produced by grains of radius $R_g = 50$ μm penetrating in water at

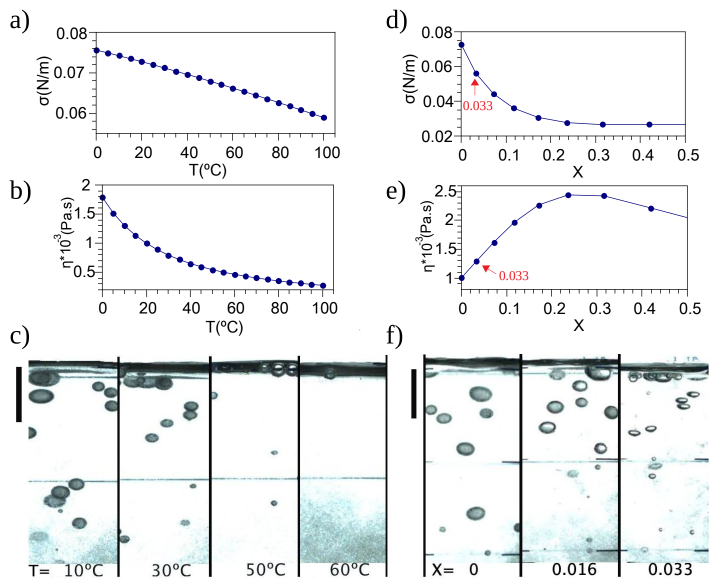

Figure 4: (a) Surface tension σ and (b) viscosity η as a function of the water temperature T. (c) Effect of water temperature on the granular bubbles: the size and number of bubbles decrease as T is increased ($R_g = 50$ μm, $h = 7.5$ cm, $X = 0$), see Movie 3 in Ref. [34]. (d) Surface tension and (e) viscosity dependence on the molar fraction of ethanol X in a binary mixture of water and ethanol. (f) Bubbles produced in bynary mixtures for three different values of X ($R_g = 50$ μm, $T = 20$°C, $h = 7.5$ cm), see Movie 4 in Ref. [34]. Plots (a), (b),(d) and (e) are based on Refs. [35, 36, 37].

different temperatures. It can be noticed that the granular bubbles are smaller at higher temperatures, *i.e.* when both parameters σ and η *decrease* [35, 36]. Above $T \sim 50$°C, granular bubbles are not observed any more. Although some air bubbles may appear, their surfaces are free of grains. The experiments at different temperatures alone do not allow us to figure out which parameter (σ or η) determines the attachment of grains because both water properties decrease with T. Thus, we decided to perform additional experiments using binary mixtures of water with different concentrations of ethanol X. Using these mixtures, we can simultaneously decrease σ and increase η by increasing X [36, 37]. At $T = 20$°C, σ *decreases* from 0.072 N/m for $X = 0$ (pure water) to ~ 0.053 N/m for $X = 0.033$, while η *increases* from 1 to 1.3 mPa.s, see Figs. 4(d)-(e). Snapshots of these experiments in Fig. 4(f) show bubbles covered with grains for $X = 0$, partially covered for $X = 0.016$ and ellipsoidal air bubbles without attached grains for $X = 0.033$. The above observations suggest that the grains stop attaching to the bubbles when the surface tension decreases, regardless of the variation of the liquid viscosity. Therefore, although η plays a role in the number, shape and size of the air bubbles, σ is the relevant liquid property in the process of particle-bubble attachment.

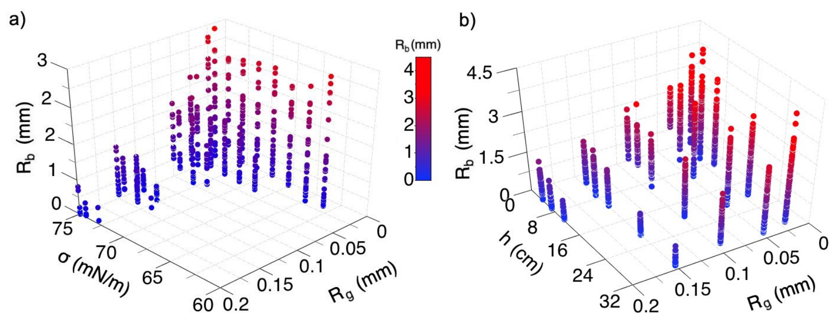

Figure 5: (a) 3D plot showing the bubble radius R_b dependence on the grain radius R_g and surface tension σ (experiments performed at constant impact velocity with $h = 7.5$ cm). (b) 3D plot showing R_b vs R_g and h (experiments performed at constant water temperature $T = 20^{\circ}$C that corresponds to $\sigma = 0.072$ N/m).

The addition of ethanol to water could aso be affecting the wettability of the glass beads, and further research tuning the wetteing properties of the material and the surface tension of the liquid independently is required. For this reason, in what follows we only consider the results obtained with pure water which are summarized in the 3D plots shown in Figure 5 (the corresponding 2D plots and additional statistical analysis can be found in the supplementary information [34]). Considering each bubble as spherical, its radius R_b was measured and plotted as a function of R_g, $\sigma(T)$ and h. Each point represents one bubble. The biggest bubbles of radius $R_b \sim 3 - 4$ mm are produced by the smallest grains. When R_g increases, the number and size of the bubbles decrease and they only form above a certain value of surface tension, see Fig. 5(a). The dependence of R_b on the impact height h does not follow a monotonous trend: it increases, decreases, remains practically constant or it is null depending on the grain size, see Fig. 5(b). Note that the number an size of bubbles is negligible for grains of radius $R_g > 150\ \mu m$; for that reason the entrained air measured in Fig. 2c was practically zero. Indeed, the volume of entrained air calculated by adding the volume of individual spherical bubbles was found in excellent agreement with the direct measure of V_{air} reported in Fig. 2c.

So far, we have delimited the experimental conditions in which the jet of glass beads produces air entrainment and granular bubbles. Let us now focus on the particle attachment process, the maximum size and stability of the bubbles, and the condition for a bubble to rise or sink inside the water pool.

3.4. Particle attachment

In the experiments performed with the smallest grains the bubbles formed were entirely covered with particles; however, for grains of radius $R_g \geqq 150\ \mu$m, we observe some bubbles partially covered with grains that accumulate towards the bottom of the encapsulate due to gravity, as illustrated in Fig. 6(a). From this picture, it appears that the the total radius of the encapsulate is the radius of the air bubble plus the diameter of the grain, *i.e.* $\sim R_b + 2R_g$. A closer view of the bubbles shown in Fig. 6(b) allows us to observe that each grain is practically attached outside of the air bubble by a capillary bridge, but no liquid bridges are visible between particles.

Figure 6(c) shows a force diagram for a particle attached to the bottom of a bubble. In the diagram, α is the half-central angle of the cone formed between the liquid bridge circumference and the center of the particle, and θ_c is the contact angle for the triple air-water-grain interface. These two angles depend on the wetting properties of the particles surface and play and important role in determining the attachment dynamics and the flotation efficiency. If water has a high contact angle on the particle surface, the attachment will be strong and the bubbles will carry the hydrophobic particles[40]. Fresh clean glass

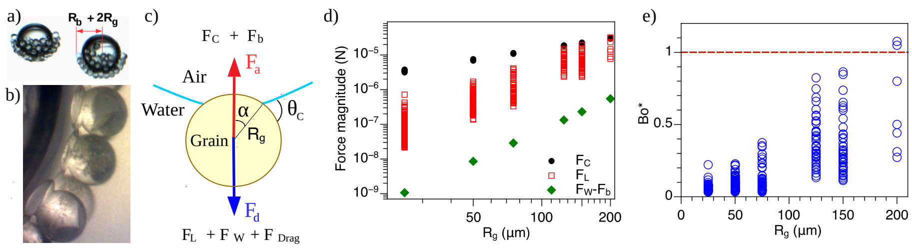

Figure 6: (a) Bubbles partially covered with grains. The total radius of the encapsulate is approximately $R_b + 2\,R_g$. (b) Picture taken with a microscope (40X) showing grains of $R_g = 150$ μm attached to the bubble by capillary bridges. (c) Force diagram for a grain attached at the bottom of a bubble (see text). (d) Magnitude of attaching and detaching forces acting on a grain attached at the bottom of the bubble. The capillary force and the Laplace pressure have similar magnitude when $R_g \approx 200\mu$m. (e) Modified Bond number Bo^* vs R_g for the data shown in (d).

surfaces are known to be hydrophilic ($\theta_c \sim 0°$) because of a high density of silanol groups which hydrogen-bond strongly with water [40, 41]. Nonetheless, a silanization process, plasma etching, or chemical treatment can be used to increase the surface hydrophobicity in a wide range. For instance, a treatment of glass beads with Dow Corning 550 silicone fluid or with hexamethyldisilazane (HMDS) allows to vary the contact angle in the range $\theta_c \sim 0 - 148°$ and $0 - 120°$, respectively [42]. In our study, we did not modify the wetting properties of the glass beads, and they were used as received from the suppliers. Since the glass beads are able to attach the air bubbles, we can assume a considerable degree of surface hydrophobicity and expect a high value of θ_c. Indeed, from pictures as the one shown in Fig. 6(b), we measured values of $\alpha \sim 30°$ and $\theta_c \sim 70°$.

But the surface wettability is not enough to ensure the particle attachment. A grain remains attached to the bubble if the attaching forces F_a along the radial direction of the bubble balance the detaching forces F_d. At the bottom of the bubble (Fig. 6c), the particles experience the larger detaching forces [43, 44]: the pressure force F_L due to the Laplace pressure difference $\Delta P = 2\sigma/R_b$, the weight of the particle F_w, and the drag force F_{drag}. On the other hand, the attaching

Force type	Expression	Range (N)
Capillary	$F_c = 2\pi\sigma R_g \sin\alpha \sin(\theta_c - \alpha)$	$10^{-6} - 10^{-5}$
Laplace	$F_L = \dfrac{2\sigma}{R_b}\pi R_g^2 \sin^2\alpha$	$10^{-7} - 10^{-5}$
Buoyancy	$F_b = \dfrac{\pi R_g^3 \rho_l g}{3}(2 + 3\cos\alpha - \cos^3\alpha)$	$10^{-8} - 10^{-6}$
Weight	$F_w = \dfrac{4}{3}\pi R_g^3 \rho_g g$	$10^{-8} - 10^{-6}$
Drag	$F_{drag} = 6\pi\eta R_g v_a$	10^{-8}

Table 2: Attaching and detaching forces acting on an individual particle at the bottom of the bubble according to the force diagram in Fig. 6(c). The order of magnitude of these forces were estimated using $\theta_c = 70°$, $\alpha = 30°$, the water density ρ_l = 998 g/cc, g =9.81m/s^2, the experimental values of R_g, σ and η, and the corresponding measured values of R_b.

forces are the capillary force F_c and the buoyant force F_b. The expressions for these forces are given in Table 2. As a first approximation, we used the Stokes drag force considering that the particles rise to the surface attached to the bubbles with a low velocity $v_a \sim \mathcal{O}(1$ cm/s), as it was measured from the videos. We estimated the magnitude of the attaching and detaching forces for each bubble of radius radius R_b produced by grains of radius R_g using the values $\alpha \sim 30°$ and $\theta_c \sim 70°$, and for the different values of surface tension. The orders of magnitude of these forces are indicated in Table 2 and Fig. 6(d). Clearly, the particle attachment is mainly determined by the capillary force and the Laplace pressure. The apparent weight $F_w - F_b$ reaches the same order of magnitude than F_c only for particles of radius $R_g \approx 1.5$ mm, considerably larger than the grains used in our experiments. Concerning F_{drag}, it is one order of magnitude smaller than the other forces and it can be neglected. Following Refs. [43, 44], we estimated the modified Bond number: $Bo^* = (F_L + F_w - F_b)/F_c$ for each bubble size as a function of R_g, see Fig. 6(e). The minimum condition $Bo^* = 1$ is the criterion for particle-bubble detachment (dashed red line). Note that $Bo^* < 1$ for most of the experimental conditions, especially for the smallest grains that produce larger bubbles, indicating that the attaching force dominates in these encapsulates. Only for grains of $R_g = 200\mu$m, some bubbles have $Bo^* \sim 1$. This occurs because those grains produce smaller bubbles and the Laplace pressure is inversely proportional to R_b; thus, F_L increases and reaches a magnitude of the same order than F_c producing particle detachment. This explains why large bubbles formed by small grains are fully covered whereas small bubbles produced by large grains are only partially covered with particles.

3.5. Maximum size of granular bubbles

Figure 7a shows the maximum bubble size R_b^{max} as a function of surface tension for different values of grain radius. It is interesting to note that grains of $R_g = 25\mu$m produce the largest bubbles with R_b^{max} (blue points) comparable to the capillary length, $\lambda_c = \sqrt{\sigma/(\rho\, g)}$ (dashed red line) for the corresponding values of surface tension. For grains of larger size, R_b^{max} decreases with σ and the bubbles stop forming at a threshold value σ_t that depends on the grain size. Even though the grains could attach to bubbles with $R_b > 3$ mm (which Laplace pressure is lower) such bubbles are not produced during the process of air entrainment. According to Ref. [9], a review about air-entrainment produced by impinging water jets, classical air bubbles in the rising bubble region have maximum diameters of 3-4 mm independently of the jet velocity and nozzle diameter. Something similar is found in our experiments: $R_b^{max} \sim 3$ mm for grains of $R_g = 25$ μm that form a more dense and collimated granular jet that looks like a liquid jet. For similar grain size, liquid-like features of a granular jet falling in air have been previously reported [38, 39, 45, 46]. As the grain size increases the jet becomes more dispersed and smaller bubbles are produced.

3.6. About the coalescence and stability of granular bubbles

Air bubbles formed in a water pool rise to the surface and coalesce with the air-water interface practically at contact [8]. Nevertheless, an air bubble can bounce below the surface for some milliseconds before coalescence [47]. Recently, it was shown that bubbles approaching to a water-air interface at very slow velocity (< 0.1 mm/s) can survive for several minutes [48]. Adjacent air bubbles also follow a fast coalescence-aggregation process [49]. In our case,

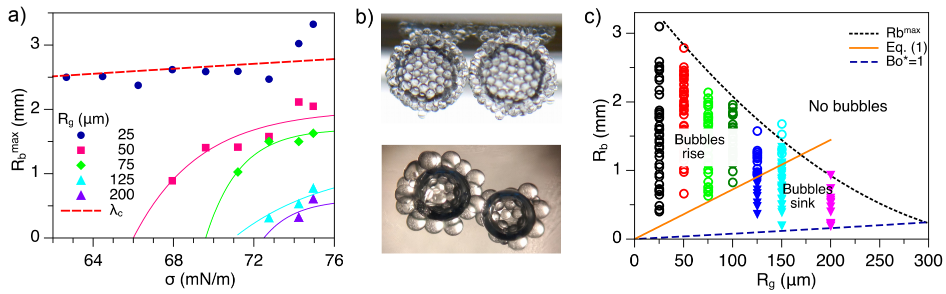

Figure 7: (a) Maximum bubble radius R_b^{max} vs σ for different values of R_g. The dashed red line corresponds to the capillary length $\lambda_c(\sigma)$. (b) Pictures of stable granular bubbles that do not coalesce between them or with the surface because they are separated by a monolayer of grains. (c) R_b vs R_g. Each empty circle or solid triangle represents a bubble that rises or sinks in the liquid pool, respectively. The orange line corresponds to the rising/sinking condition given by equation (1). Bubbles are not produced for values above the dotted black line (a reference to the eye).

the bubbles are considerably stable due to the existence of a grain monolayer that prevents coalescence between adjacent bubbles or between the bubbles and the interface, see Fig. 7b. The life-time of granular bubbles can be extended to several days. On the other hand, it is important to remark some differences between the granular bubbles reported here and the air bubbles stabilized using poly(tetrafluoroethylene) micropowder dispersed in oil [50] or with nanometric silica particles dispersed in water [51]. In such studies, the bubbles formed are micrometric in size and produced by direct injection of air into the liquid. Moreover, the particles must be dispersed to allow their rapid migration to the air-water interfaces [51] and the particle weight must be negligible to remain suspended forming an air-oil emulsion [50] or just below the water surface [51]. In our case, the air entrainment and the bubbles are generated by the same granular jet (a simpler method), the bubbles are considerably larger (of the order of millimeters), and the weight of the grains can be large enough to make the bubbles sink when its magnitude surpasses the buoyant force. The condition for bubble flotation depending on the grain size is presented in the next section.

3.7. Rising or Sinking condition for a granular bubble.

Let us assume as a good approximation a perfectly spherical bubble of radius R_b totally covered by a monolayer of N glass beads of radius R_g. The total area covered by grains is the surface of a sphere of radius $R_b + R_g$, with particle surface fraction: $\phi = N\pi R_g^2/4\pi(R_b + R_g)^2$. Then, the number of particles attached to the bubble is $N \approx 4\phi(R_b + R_g)^2/R_g^2$. Defining V_g as the volume of one bead, a granular bubble of volume $V_b = (4/3)\pi R_b^3 + NV_g$ will rise (resp. sink) in the liquid if the buoyant force B is larger (resp. smaller) than the weight of the encapsulate W given by the weight of the air bubble W_{air} plus the weight of the attached grains W_{grains}. Since $W = W_{air} + W_{grains} \approx W_{grains} = N\frac{4}{3}\pi R_g^3\rho_g g$, and $B = \rho_l g V_b = \frac{4}{3}\pi\rho_l g\left(R_b^3 + 4\phi(R_b + R_g)^2 R_g\right)$, the condition for the equilibrium $B = W$ is satisfied by:

$$R_b{}^3 - 4\phi\frac{\rho_g - \rho_l}{\rho_l}(R_b + R_g)^2 R_g = 0. \tag{1}$$

Using $\phi = 0.84$ for a two-dimensional hexagonal lattice of monodisperse beads, the condition given by Eq. (1) is plotted together with the experimental data in Fig. 7c. Note that the measured radius of bubbles rising to the surface (open circles) and sinking to the bottom of the pool (solid triangles) are separated in two zones well-predicted by the proposed model (solid orange line). This model-experiment agreement supports our assumption of spherical bubbles with particles practically attached outside the bubble surface.

4. Conclusions

We have studied the impact and penetration of a granular jet falling into water. Although the dynamics of dry granular jets moving in air and impacting in solid surfaces has been previously addressed [45, 38, 39], this is the first systematic study focused on a submerged granular jet. During its penetration, the jet deforms the air-water interface and produces air entrainment that leads to the formation of bubbles covered with grains. The required conditions for air entrapment and bubble formation were determined experimentally for a jet of glass beads. This is an important first step considering that determining such conditions for the case of a water jet penetrating into the same liquid has been challenging during decades [1, 9, 10, 11]. We show that the volume of air entrained is linearly proportional to the volume of poured grains and decreases as the grain size is increased, being negligible for particles $> 300\mu$m. The largest granular bubbles formed in the process are found similar in size to air bubbles generated by a water jet ($R_b \sim 3$ mm [9]), but the former are considerably more stable because the monolayer of grains prevents coalescence. The stability of these bubbles is unexpected considering the relatively large grain size compared to previous studies [51] and that surfactants or liquid thickeners were not used [27]. Moreover, the granular bubbles not only rise, they can also sink if the weight of the assembly is larger than the buoyant force. This can be used for gas storage at the bottom of a water reservoir. The above mechanism can also be applied as a simple and inexpensive technique for stabilizing bubbles and foams. Since the process of air entrainment by plunging (liquid or granular) jets is relevant in many natural and industrial scenarios [1, 15, 16], the community will be interested in investigating further how our findings depend on the shape and wetting properties of the grains and the nature of the gas-liquid interface.

Acknowledgments

This research was supported by CONACYT Mexico and the VIEP-BUAP project 2019. AMCA and YYEO thank the PhD scholarships provided by CONACYT Mexico.

[1] K. T. Kiger, J. H. Duncan, Air-Entrainment Mechanisms in Plunging Jets and Breaking Waves, Annu. Rev. Fluid Mech. 44 (2012) 563-596.

[2] Handbook of industrial water treatment, General Electric Company 1997-2012.

[3] X F Ge et al., Study on pressure drop and cavitation performance of ro-

tating disk at different speeds, IOP Conf. Ser.: Earth Environ. Sci. 163, 012099 (2018).

[4] T. Tran, H. de Maleprade, C. Sun, D. Lohse, Air entrainment during impact of droplets on liquid surfaces, J. Fluid Mech.726 (2013) 3.

[5] A.-B. Wang, C.-C. Kuan, and P.-H: Tsai, Do we understand the bubble formation by a single drop impacting upon liquid surface? Physics of Fluids 25, 101702 (2013)

[6] Pumphrey, H. C., Crum, L. A., Bjono, L. Underwater sound produced by individual drop impacts and rainfall. J. Acoust. Soc. Am. 85, 1518-26 (1989).

[7] A. Prosperetti and H. N. Oguz, The impact of drops on liquid surfaces and the underwater noise of rain, Annu. Rev. Fluid Mech. 25, 577-602 (1993)

[8] H.N. Oguz, A. Prosperetti, A. Lezzi, Examples of air-entraining flows, Physics of Fluids A: Fluid Dynamics 4 (1992) 649-651.

[9] A.K. Bin, Gas entrainment by plunging liquid jets, Chemical Engineering Science 48(21) (1993) 3585-3630.

[10] M. El Hammoumi, J. L. Achard, L. Davoust, Measurements of air entrainment by vertical plunging liquid jets. Exp. Fluids 32 (2002) 624-38

[11] E. J. McKeogh, D. A. Ervine, Air entrainment rate and diffusion pattern of plunging liquid jets. Chem. Eng. Sci. 36 (1981) 1161-72

[12] J. Ciborowski, A. Bin, Minimum entrainment velocity for free liquid jets. Inz. Chem 2 (1972) 557-77.

[13] J.M. Aristoff, J.W.M. Bush, Water entry of small hydrophobic spheres, Journal of Fluid Mechanics 619 (2009) 45-78.

[14] D. Vella, Floating Versus Sinking, Annu. Rev. Fluid Mech. 47 (2015) 115-135.

[15] P. C. Fonseca, G. W. Scherer, An image analysis procedure to quantify the air void system of mortar and concrete, Mater Struct (2015) 48: 3087.

[16] S. Viroulet, A. Sauret, O. Kimmoun, Tsunami generated by a granular collapse down a rough inclined plane, EPL 105 (2014) 34004.

[17] S. Nowak, A. Samadani, A. Kudrolli, Maximum angle of stability of a wet granular pile, Nat. Phys. 1 (2005) 50-52.

[18] N. Mitarai, F. Nori, Wet granular materials, Adv. Physics 55 (2006) 1-45.

[19] S. Strauch, S. Herminghaus, Wet granular matter: a truly complex fluid, Soft Matter 8 (2012) 8271-8280.

[20] M. Pakpour, M. Habibi, P. Moller, D. Bonn, How to construct the perfect sandcastle, Scientific Reports 2 (2012) 549.

[21] F. Pacheco-Vázquez, F. Moreau, N. Vandewalle, S. Dorbolo, Sculpting sandcastles grain by grain: Self-assembled sand towers, Phys. Rev. E 86 (2012) 051303.

[22] G. Saingier, A. Sauret, P. Jop, Accretion Dynamics on Wet Granular Materials, Phys. Rev. Lett. 118 (2017) 208001.

[23] Y. Yang, *et. al*, An Overview of Pickering Emulsions: Solid-Particle Materials, Classification, Morphology, and Applications, Front. Pharmacol. 8 (2017) 287.

[24] P. Aussillous, D. Quéré, Liquid marbles, Nature 411 (2001) 924-927.

[25] L. Mahadevan, Y. Pomeau, Rolling droplets, Phys. Fluids 11 (1999) 2449-2453.

[26] T. Supakar, A. Kumar, J.O. Marston, Impact dynamics of particle-coated droplets, Phys. Rev. E 95 (2017) 013106.

[27] Y. Timounay, O. Pitois, F. Rouyer, Gas Marbles: Much Stronger than Liquid Marbles, Phys. Rev. Lett 118 (2017) 228001.

[28] A.B. Subramaniam, M. Abkarian, L. Mahadevan, H.A. Stone, Colloid science: non-spherical bubbles, Nature 438(7070) (2005) 930.

[29] M. Abkarian, A.B. Subramaniam, S.H. Kim, R.J. Larsen, S.M. Yang, H.A. Stone, Dissolution arrest and stability of particle-covered bubbles, Phys. Rev. Lett 99 (2007) 188301.

[30] A.B. Subramaniam, M. Abkarian, H. A. Stone, Controlled assembly of jammed colloidal shells on fluid droplets, Nature Mater. 4 (2005) 553-556.

[31] M. Abkarian, S. Protière, J.M. Aristoff, H.A. Stone, Gravity-induced encapsulation of liquids by destabilization of granular rafts, Nature Comms. 4 (2013) 1895.

[32] S. Protiere, C. Josserand, J.M. Aristoff, H.A. Stone, M. Abkarian, Sinking a Granular Raft, Phys. Rev. Lett. 118 (2017) 108001.

[33] E. Bormashenko, Liquid marbles: Properties and applications, Current Opinion in Colloid and Interface Science 16 (2011) 266-271.

[34] See Supplementary Information and Videos at [Please insert link].

[35] L. Korson, W. Drost-Hansen, F.J. Millero, Viscosity of water at various temperatures, Journal of Physical Chemistry 73 (1969) 34-39.

[36] I.S. Khattab, F. Bandarkar, M.A.A. Fakhree, A. Jouyban, Density, viscosity, and surface tension of water+ethanol mixtures from 293 to 323K, Korean J. Chem. Eng. 29(6) (2012) 812-817.

[37] G. Vázquez, E. Álvarez, J.M. Navaza, Surface Tension of Alcohol Water + Water from 20 to 50 .degree.C, J. Chem. Eng. Data 40(3) (1995) 611-614.

[38] Z.-H. Shi, W.-F. Li, W.-W. Qian, H.-F. Liu, F.-C. Wang, Liquid-like granular film from granular jet impact, Chem. Eng. Sci. 162 (2017) 1-9

[39] G. Prado, Y. Amarouchene, H. Kellay, Experimental Evidence of a Rayleigh-Plateau Instability in Free Falling Granular Jets, Phys. Rev. Lett. 106 (2011) 198001.

[40] R. M. Pashley, M. E. Karman (John Wiley & Sons, Ltd. 2004) p.p 168-169.

[41] L. Holland, Properties of glass surfaces (Wiley, New York, 1964) p.359

[42] A. K. Singhal, P. M. Dranchuk, Wettability Control of Glass Beads, Can. J. Chem Eng. 53 (1975)

[43] G. Wang, D. Feng, A. Nguyen, G.M. Evans, The dynamic contact angle of a bubble with an immersed-in-water particle and its implications for bubble-particle detachment, Int. J. Miner. Process. 151 (2016) 22-32.

[44] G. Wang, A.V. Nguyen, S. Mitra, J.B. Joshi, G.J. Jameson, G.M. Evans, A review of the mechanisms and models of bubble-particle detachment in froth flotation, Separation and Purification Technology 170 (2016) 155-172.

[45] X. Cheng, G. Varas, D. Citron, H. M. Jaeger, S. Nagel, Collective behavior in a granular jet: Emergence of a liquid with zero surface tension, Phys. Rev. Lett. 99 (2007) 188001.

[46] A. M. Cervantes-Álvarez, S. Hidalgo-Caballero, and F. Pacheco-Vázquez, The simultaneous discharge of liquid and grains from a silo, Physics of Fluids 30 (2018) 043302.

[47] J. Zawala, K. Malysa, Influence of the impact velocity and size of the film formed on bubble coalescence time at water surface, Langmuir 27(6) (2011) 2250-2257.

[48] L.A. del Castillo, S. Ohnishi, R.G. Horn, Inhibition of bubble coalescence: Effects of salt concentration and speed of approach, Journal of Colloid and Interface Science 356 (2011) 316-324.

[49] E. Villermaux, Fragmentation, Annu. Rev. Fluid Mech. 39 (2007) 419-446.

[50] B. P. Binks, Anais Rocher, Stabilisation of liquid-air surfaces by particles of low surface energy, Phys. Chem. Chem. Phys., 12, (2010) 9169-9171.

[51] Du et al., Outstanding Stability of Particle-Stabilized Bubbles, Langmuir (2003), 19, 8, 3106-3108.

Supplementary information

Air entrainment and granular bubbles generated by a jet of grains entering water.

A. M. Cervantes-Alvarez[1], Y.Y. Escobar-Ortega[1], A. Sauret[2] and F. Pacheco-Vázquez[1]

[1] *Instituto de Física, Benemérita Universidad Autónoma de Puebla, A. P. J-48, Puebla 72570, México.*

[2] *Department of Mechanical Engineering, University of California, Santa Barbara, CA 93106, USA*

1. Dependence of the volume of entrained air on the impact height:

When a granular jet enters into water, the relative velocity between the liquid and the jet generates an instability that leads to the bending of the jet, see Supplementary Fig. 1(a). The wavelength λ of the instability has a value close to $\lambda \approx 5$ mm. When the amplitude of the instability grows deep in the pool, the granular jet breaks up into several bubbles covered with grains that keep the entrained air encapsulated. The volume of air V_{air} entrained by the granular jet was determined by measuring the change in the water level inside the cylindrical container after pouring a known volume of grains from different heights. The dependence of V_{air} on the impact height h is shown in Supplementary Figs. 1(b)-(c).

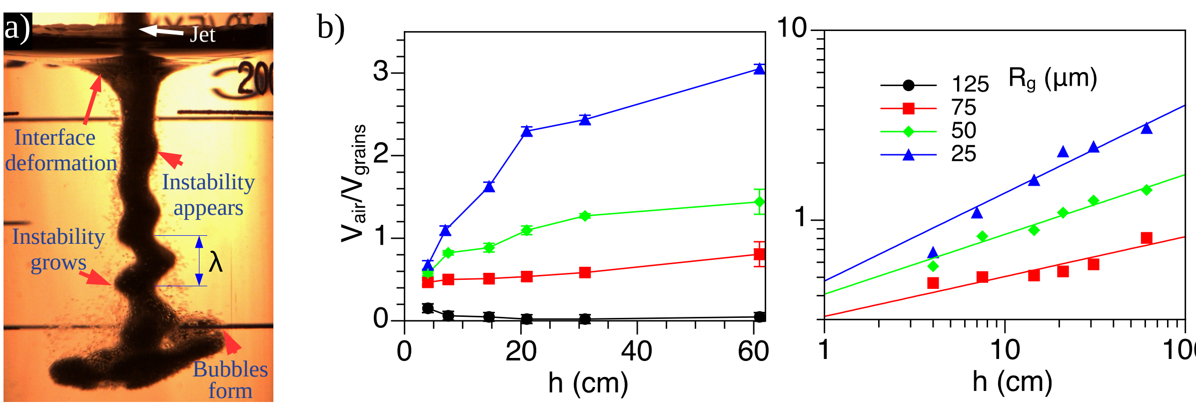

Supplementary Fig. 1. a) Picture showing the formation of instabilities produced by the granular jet penetrating into water. This instability appears due to the relative motion of the granular jet with respect to the quiescent water (similar to the Kelvin-Helmholtz instabilities for two fluids). b) Ratio of the volume of entrained air with the volume of poured grains, V_{air}/V_{grains}, as a function of the impact height, h, for grains of different radius. For a given grain size, V_{air}/V_{grains} increases with h. Nevertheless, for grains of radius $R_g = 125$ μm, the amount of air entrained goes rapidly to zero when h increases. For larger grains, V_{air} is negligible. c) Log-log plot indicating a power dependence of the form: $V_{air}/V_{grains} = Ah^p$, where A is a constant. The blue line has a slope $p = 0.5$, and for that case $V_{air}/V_{grains} \propto \sqrt{h}$, since $v = \sqrt{2gh}$, one finds that $V_{air}/V_{grains} \propto v$. Nevertheless, the exponent p is strongly dependent on the grain size and its value decreases for larger grains. For that reason, the data scaling in terms of dimensionless numbers (for instance, the Weber number or capillary number) is not straightforward.

2. Mole fraction concentration X in binary mixtures of water and ethanol

This section describes how the values of X reported in the main manuscript were obtained. The molar fraction X_i represents the ratio of the number of moles of one component n_i to the number of moles of all components n_{total} present in a mixture:

$$X_i = \frac{n_i}{n_{total}}.$$

The number of moles is given by: $n_i = m_i/M_i$, where m_i represents the mass of the component and M_i the molar mass. In a binary mixture of water and ethanol, we have that:

$$X_{ethanol} = \frac{n_{ethanol}}{n_{ethanol} + n_{water}}.$$

Considering the density of ethanol $\rho_{ethanol}$=0.789 g/ml and the density of water ρ_{water}=0.997 g/ml, for a mixture of a volume of water $V_{water} = 95$ ml and $V_{ethanol} = 5$ ml, we have:

$$n_{ethanol} = \frac{m_{ethanol}}{M_{ethanol}} = \frac{\rho_{ethanol} V_{ethanol}}{M_{ethanol}} = \frac{3.945\text{g}}{46.07\text{g/mol}} = 0.086$$

and:

$$n_{water} = \frac{m_{water}}{M_{water}} = \frac{\rho_{water} V_{water}}{M_{water}} = \frac{94.715\text{g}}{18.02\text{g/mol}} = 5.256$$

Therefore:

$$X_{ethanol}(5\%) = \frac{0.086}{0.086 + 5.256} = 0.016$$

From a similar calculation for a mixture of 90 ml water plus 10 ml ethanol, we obtain $n_{ethanol} = 0.171$ mol and $n_{water} = 4.98$ mol. Therefore:

$$X_{ethanol}(10\%) = \frac{0.171}{0.171 + 4.980} = 0.033$$

3. Measuring the radius of the granular bubbles:

Granular bubbles produced in pure water can be assumed to be spherical according to our observations of stable bubbles that reach the water-air interface, see Supplementary Fig. 2a. When the bubbles are rising through the water, they present small variations from the spherical shape due to the liquid drag, see Supplementary. Fig. 2b. Only the bubbles generated in binary mixtures of water and ethanol with X=0.033 are considerably oblate during its ascent phase through the liquid (see Supplementary Fig. 2c), but these bubbles are not covered by grains and they were ignored in the analysis of the bubble size. This shape could be due to the increase of the liquid viscosity that augments the drag force, accompanied by the simultaneous decrease of surface tension (see the dependences of σ and η with X in Fig. 4 of the main manuscript).

In some cases, the shape of some granular bubbles in pure water seems to be also considerably oblate close to the lateral wall of the container. However, this artifact is caused by optical distortion since our experiments are performed in a cylindrical glass tube. Most of the granular bubbles generated in our experiments are quite small (less than 3 mm, smaller than the capillary length) and have a spherical shape. As an exercise, we calculated the volume of entrained air by adding the volume of bubbles assuming spherical shapes with radius R_b, and it was compared to the volume measured directly by the change of the liquid level, obtaining very close results, confirming that the assumption of spherical bubbles is a good approximation.

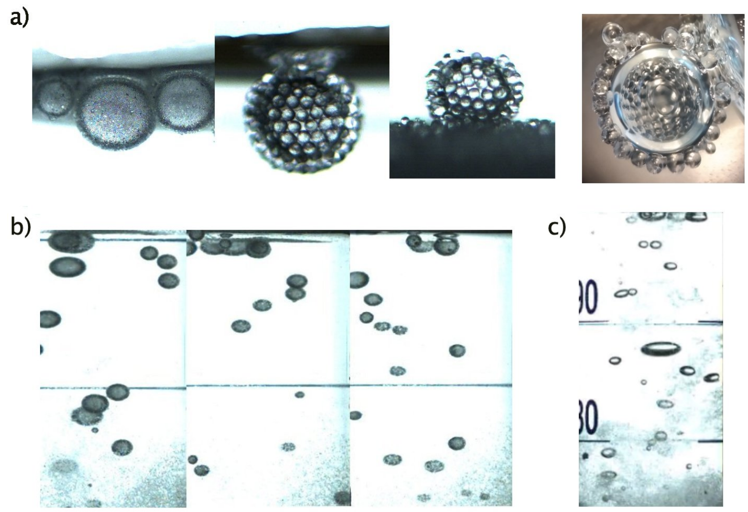

Supplementary Fig. 2. a) Static granular bubbles practically adopt a spherical shape. b) Granular bubbles rising in water are considerably spherical, only a small deformation is produced by the liquid drag. c) Air bubbles rising in a binary mixture of water with 10% volume of ethanol are considerably deformed and adopt an oblate spheroidal shape.

In order to determine the radius of the granular bubbles R_b, we measured from the videos the projected perimeter P and the circularity of the bubbles using ImageJ, and then the radius was obtained as $R_b = P/(2\pi)$. Most of the bubbles have a circularity larger than 0.95, justifying the assumption of the spherical approximation. After obtaining the radius of each encapsulate, we subtracted from it the diameter of the grains used to generate the bubbles considering that the grains are attached practically outside the air bubble. This procedure was repeated for the different values of grain size and impact velocity.

Supplementary Figure 3 shows the results of R_b as a function of the grain radius for jets penetrating into water at different temperatures. As it is discussed in the main manuscript, the bubble size decreases when the grain size increases in all cases. Moreover, the bubbles stop forming above a certain temperature depending on the grain size. For instance, for $T = 40°$C, grains of $R_g > 50\ \mu m$ do not produce bubbles. Only the grains of $R_g = 25\ \mu m$ are able to form bubbles in the complete range of liquid water temperatures.

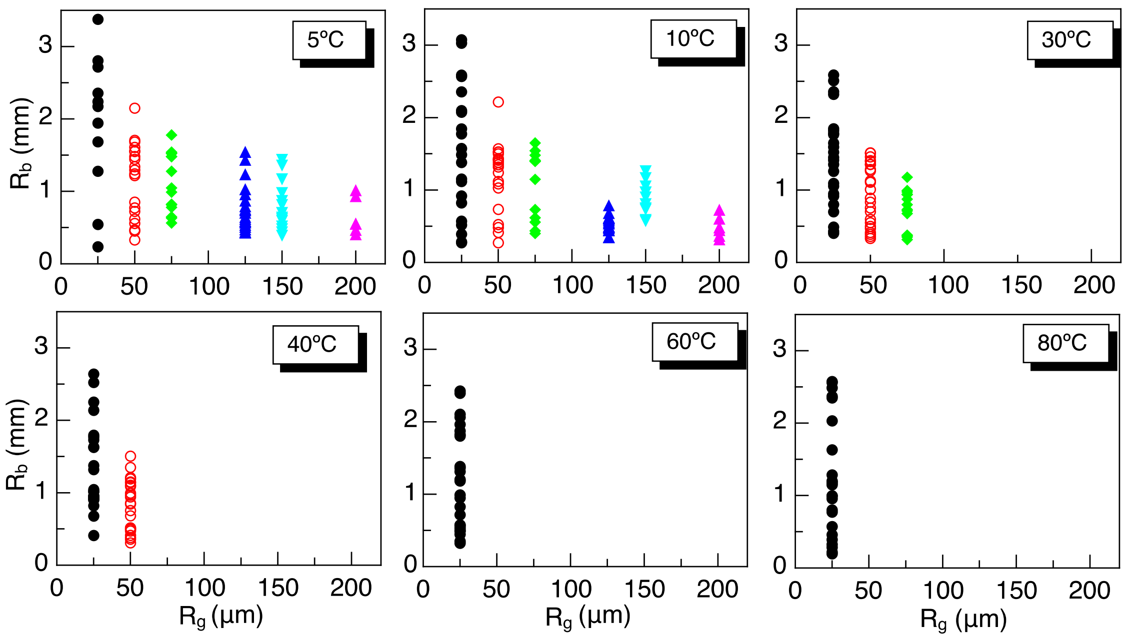

Supplementary Fig. 3. a) Bubble radius R_b vs grain radius R_g for different water temperatures T. Each point represents one bubble, and the same color is used a reference of the same grain size in all the panels.

When the temperature of water increases, its surface tension σ decreases [2, 3]. In Supplementary Fig. 4, the average size and the median size of the granular bubbles are plotted as a function of σ for four different values of grain size. Surface tension plays a fundamental role in the attaching mechanism of grains by capillary bridges. Large grains cannot remain attached to the bubbles for low values of surface tension.

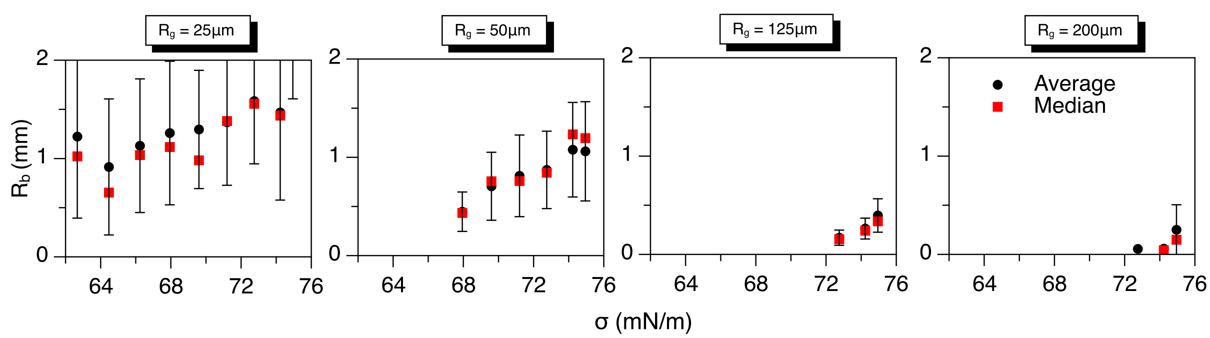

Supplementary Fig. 4. Average radius and median radius of bubbles as a function of the water surface tension for different values of grain size (indicated above of the plots).

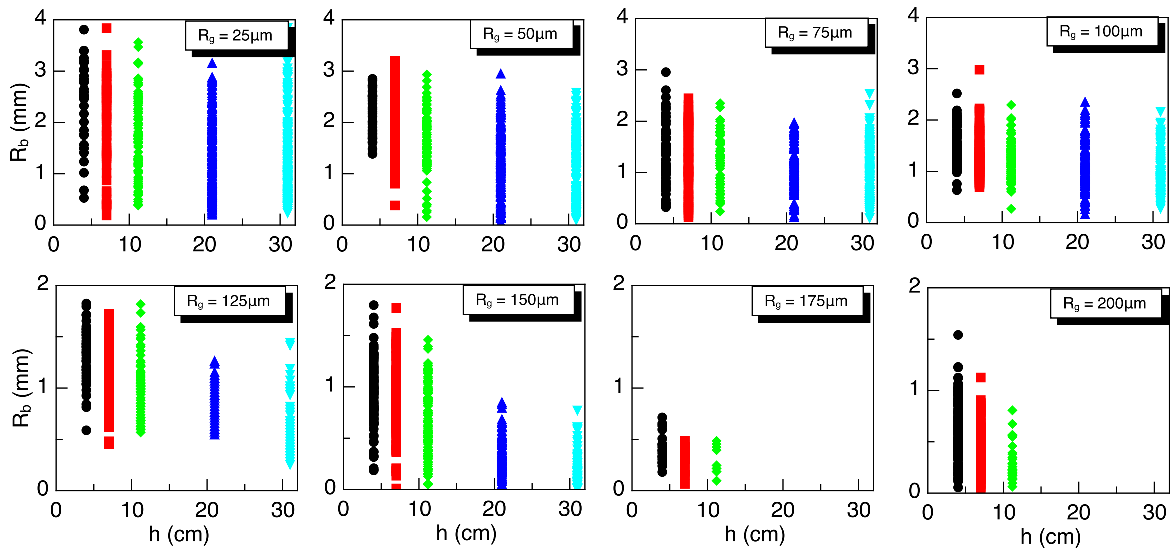

Supplementary Fig. 5. a) Bubble radius R_b vs impact height h for different values of grain size R_g. Each point represents one bubble.

The effect of the impact velocity of the granular jet on the amount of entrained air and on the size of the granular bubbles was also investigated. To vary the impact height, the grains were poured from different heights h. Supplementary Fig. 5 shows the results of R_b as a function of h in the range $0 < h < 31$ cm for different grain sizes. For the smallest grains, the bubble radius takes values between 0 and 4 mm, and this range becomes narrower as h increases and for larger grains. Moreover, we can also observe that the bubbles stop forming when $h > 11$ cm for grains of 175 and 200 μm. The average radius and the median radius of the bubbles depending on h are plotted in Supplementary Fig. 6.

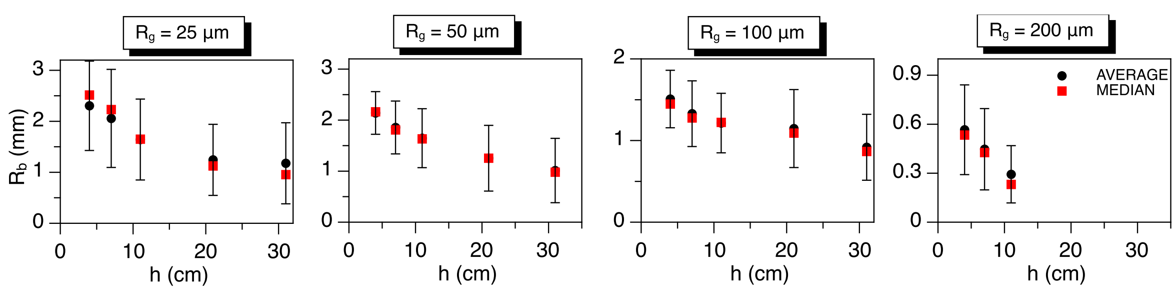

Supplementary Fig. 6. Average radius and median radius of bubbles as a function of h for different values of grain size (indicated above of the plots).

The number of bubbles formed in the process also varies with the impact height. Supplementary Fig. 7 shows the size distribution of bubbles, where N represents the number of bubbles of a given size R_b. Note that the number of bubbles is considerably larger for the case $R_g = 25\mu$m for all the values of h, and that N decreases substantially for larger grain size. The total number of bubbles N_{tot} as a function of h increases for the smaller grains (see the cases $R_g = 25$ μm, and 50 μm), remains almost constant for $R_g = 100\mu$m and decreases for $R_g = 200$ μm. The above results reveal the complex dependence of the bubble size on the impact velocity of the grains.

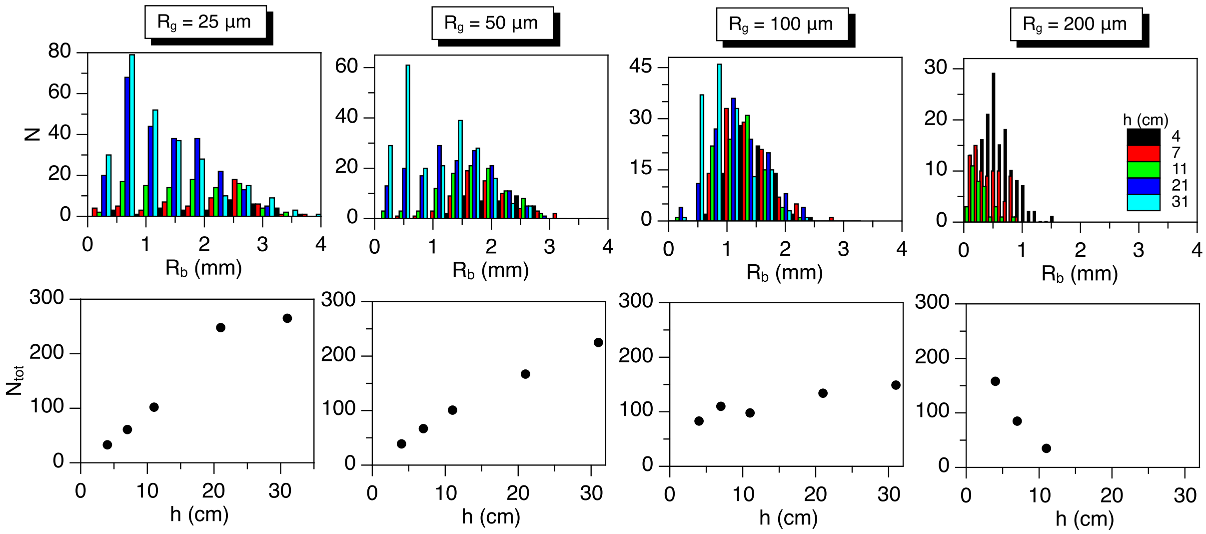

Supplementary Fig. 7. Number of bubbles N produced by grains of a given size poured form different heights h. Depending on the grain size, the total number of bubbles N_{tot} increases, remains practically constant, or decreases with h.

4. Measuring of the liquid bridge half-angle α and the contact angle θ_c.

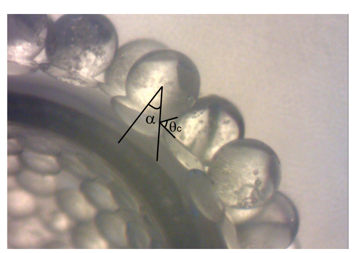

Supplementary Fig. 8. The angles α and θ_c were estimated using ImageJ from pictures taken with a microscope, as the one shown in this figure. These angles were used to calculate the magnitude of attaching and detaching forces acting on the particles. The results are reported in Table 2 of the main manuscript.

5. Effect of the grain size on the maximum size of granular bubbles:

The upper color points of Supplementary Fig. 5 indicate the maximum size R_b^{max} of the bubbles produced by grains of a certain size. In each case, the average of the five largest bubbles was calculated and plotted as a function of R_g in Supplementary Fig. 9. Clearly, R_b^{max} decreases when R_g increases. Note also that the bubbles only form for grains that a given size, and this threshold radius decreases as the temperature is increased.

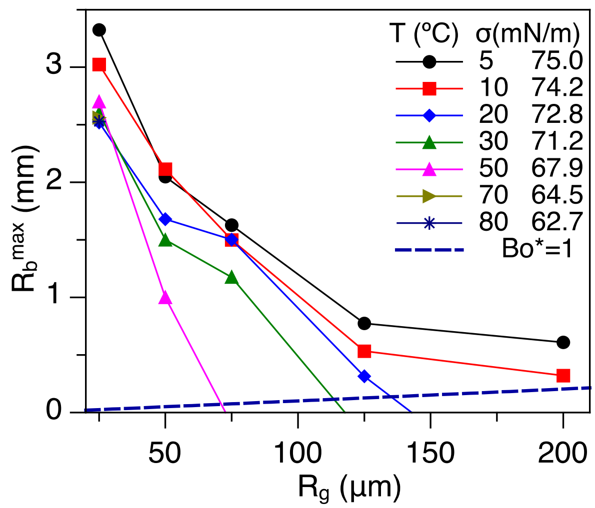

Supplementary Fig. 9 Maximum bubble size R_b^{max} for different values of grain radius R_g and temperature T. The corresponding values of surface tension σ are indicated. The dashed blue line corresponds to $Bo* = 1$ and indicates that below that line the grains detach from the surface of the bubble because the detaching forces overcome the attaching forces.

[1] L. Korson, W. Drost-Hansen, and F. J. Millero, The Journal of Physical Chemistry, **73** (1969) 34-39
[2] I. S. Khattab, F. Bandarkar, M. A. A. Fakhree, and A. Jouyban, Korean J. Chem. Eng. **29**(6), (2012) 812-817
[3] G. Vázquez, E. Álvarez, and J.M. Navaza, J. Chem. Eng. Data 40 611-614 (1995).